

Estimating aircraft drag polar using open flight surveillance data and a stochastic total energy model

Sun, Junzi; Hoekstra, Jacco; Ellerbroek, Joost

DOI

[10.1016/j.trc.2020.01.026](https://doi.org/10.1016/j.trc.2020.01.026)

Publication date

2020

Document Version

Final published version

Published in

Transportation Research. Part C: Emerging Technologies

Citation (APA)

Sun, J., Hoekstra, J., & Ellerbroek, J. (2020). Estimating aircraft drag polar using open flight surveillance data and a stochastic total energy model. *Transportation Research. Part C: Emerging Technologies*, 114, 391-404. <https://doi.org/10.1016/j.trc.2020.01.026>

Important note

To cite this publication, please use the final published version (if applicable).
Please check the document version above.

Copyright

Other than for strictly personal use, it is not permitted to download, forward or distribute the text or part of it, without the consent of the author(s) and/or copyright holder(s), unless the work is under an open content license such as Creative Commons.

Takedown policy

Please contact us and provide details if you believe this document breaches copyrights.
We will remove access to the work immediately and investigate your claim.

Green Open Access added to TU Delft Institutional Repository

'You share, we take care!' – Taverne project

<https://www.openaccess.nl/en/you-share-we-take-care>

Otherwise as indicated in the copyright section: the publisher is the copyright holder of this work and the author uses the Dutch legislation to make this work public.



Estimating aircraft drag polar using open flight surveillance data and a stochastic total energy model

Junzi Sun*, Jacco M. Hoekstra, Joost Ellerbroek

Faculty of Aerospace Engineering, Delft University of Technology, Kluyverweg 1, 2629 HS Delft, the Netherlands

ARTICLE INFO

Keywords:

Aircraft performance
Drag polar
Aerodynamic coefficient
Bayesian computing
MCMC
Stochastic total energy model

ABSTRACT

In air traffic management research, aircraft performance models are often used to generate and analyze aircraft trajectories. Although a crucial part of the aircraft performance model, the aerodynamic property of aircraft is rarely available for public research purposes, as it is protected by aircraft manufacturers for commercial reasons. In many studies, a simplified quadratic drag polar model is assumed to compute the drag of an aircraft based on the required lift. In this paper, using surveillance data, we take on the challenge of estimating the drag polar coefficients based on a novel stochastic total energy model that employs Bayesian computing. The method is based on a stochastic hierarchical modeling approach, which is made possible given accurate open aircraft surveillance data and additional analytical models from the literature. Using this proposed method, the drag polar models for 20 of the most common aircraft types are estimated and summarized. By combining additional data from the literature, we propose additional methods allowing aircraft total drag to be calculated under other configurations, such as when flaps and landing gears are deployed. We also include additional models allowing the calculation of wave drag caused by compressibility at high Mach number. Though uncertainties exist, it has been found that the estimated drag polars agree with existing models, as well as CFD simulation results. The trajectory data, performance models, and results related to this study are shared publicly.

1. Introduction

Since the invention of aircraft, researchers have been studying the aerodynamic properties of airfoils and aircraft. Examples of fundamental studies on aerodynamic drag are given by [Hoerner \(1951, 1958\)](#). From the start, the main goal has been to optimize the lift over drag ratio. Much effort has been dedicated to creating designs that would reduce drag and increase the lift efficiency of aircraft. Being able to accurately model the lift and drag is important to understand the performance of the modern aircraft and in turn, support a variety of studies in the air transportation research domain.

In general, lift and drag forces of an aircraft are considered as functions of the wing area, dynamic airspeed, and air density, and the remaining effects of the flow for both the lift and drag are described with coefficients for both forces. The most challenging aspect is to accurately calculate the lift and drag coefficients. They are dependent on the Mach number, the angle of attack, boundary layer, and, ultimately, on the aircraft aerodynamic shape. For fixed-wing aircraft, these coefficients are often modeled as functions of the angle of attack, which is the angle between the aircraft body axis and the airspeed vector. Though a more complex dynamic model involves six degrees of freedom can be used, for most of the air traffic management (ATM) research, the simplified point-mass aircraft

* Corresponding author.

E-mail address: j.sun-1@tudleft.nl (J. Sun).

<https://doi.org/10.1016/j.trc.2020.01.026>

Received 29 May 2019; Received in revised form 21 December 2019; Accepted 28 January 2020
0968-090X/ © 2020 Elsevier Ltd. All rights reserved.

performance model can be applied. This model considers an aircraft as a point mass, where the angle of attack, as well as the side-slip angle and the effect of the angular rates, are not explicitly considered. While simplifying the aircraft dynamic as a point mass model, it is also common to use *drag polar* to express the relationship between the drag coefficient and lift coefficient, making it one of the main factors describing the performance of an aircraft in many studies. Knowledge of the drag polar is therefore essential for ATM studies on such topics as trajectory prediction, fuel optimization, and state estimation.

Several methods focus on modeling the aerodynamics exists for exploring the aircraft performance during the preliminary design phase. Hence, one public source of information regarding drag polar models comes from textbooks related to aircraft designs (Anderson, 1999; Ruijgrok, 2009; Obert, 2009; Torenbeek, 1976). However, very often, only older aircraft models and extrapolations of similar designs are available in the literature. For example, in van Es (2002), an empirical model for estimating zero-lift drag coefficients was proposed using existing literature data based on several aircraft models. In general, open data on drag polar models are rare, especially for modern commercial aircraft.

The aircraft manufacturers who design the aircraft do have accurate aerodynamic data that can be used to construct the drag polar model. However, these data are generally not publicly available due to commercial considerations. Currently, the most comprehensive collection of drag polar data is the Base of Aircraft Data (BADA), which is constructed based on reference flight data and information provided by aircraft manufacturers. It contains drag polar models for most aircraft types. BADA is the default “go-to” aircraft performance model for current ATM studies, which can currently be obtained with a project-based license.

The goal of this paper is to propose an alternative path for estimating the drag polars of modern commercial aircraft, which do not rely on proprietary data. We approach this estimation problem using a novel stochastic total energy (STE) model. The STE approach treats the parameters of the standard total energy model as random variables. With this stochastic model, we consider the parameter estimation problem as a minimization problem using Bayesian computing, specifically, the Markov Chain Monte Carlo (MCMC) approximations. The application of this Bayesian approach is slowly being brought to the engineering domain. For example, Nagel and Sudret (2015) outlined a multi-level system estimation application using such a hierarchical model approach. The STE model and solutions proposed in this paper are closely related to this line of research. Finally, using this method, a collection of drag polars for common airliners are produced and made publicly available by this paper.

The structure of this paper is as follows. In section two, the fundamentals of the point-mass drag polar model are introduced. In section three, we focus on the hierarchical stochastic model approach and the solution using MCMC. In section four, different factors that alter the drag polar are studied. In section five, experiments are conducted to examine and obtain drag polar models. Section six gives summaries and discussions regarding the results. The conclusions regarding this study are made in section seven.

2. Definition of the drag polar in point-mass models

When an aircraft flies, the resulting aerodynamic force can be presented as two orthogonal components, which are lift and drag. The drag is produced by the airflow interacting with the aircraft body. The lift is the result of a pressure difference between the upper and lower surface of the lifting devices (wings). With the same airspeed and altitude conditions, control of lift is performed by changing the aircraft angle of attack and/or modifying the surface shape of the lifting devices. By changing the elevator settings, the pitch angle and the angle of attack can be controlled. On the other hand, a change of the lifting device surface to increase the lift is primarily performed by re-configuring the flaps.

In general, the lift and drag forces of an aircraft that is traveling through a volume of air with free stream velocity V can be computed as:

$$\begin{aligned} L &= C_L q S \\ D &= C_D q S \\ q &= \frac{1}{2} \rho V^2 \end{aligned} \quad (1)$$

where C_L and C_D are lift and drag coefficients, respectively. q is the dynamic pressure. ρ , V , and S are air density, true airspeed, and the lifting surface area of the aircraft. In practice, C_L and C_D can be modeled as functions of the angle of attack (α), Mach number (M), and flap deflection (δ_f):

$$\begin{aligned} C_L &= f_{cl}(\alpha, M, \delta_f) \\ C_D &= f_{cd}(\alpha, M, \delta_f) \end{aligned} \quad (2)$$

In aerodynamic models, multi-dimensional table interpolation or higher-order polynomials are often used to express these functions. However, in many ATM studies, a point-mass model is only required, where the angle of attack is not modeled, while the effect of Mach number and flap deflection are considered as additional factors.

In the point-mass performance model, the relation between the aerodynamic coefficients C_D and C_L can be simplified to the drag polar. The simplest form of drag polar describes a quadratic relationship that can be model as:

$$C_D = C_{D0} + k C_L^2 \quad (3)$$

where C_{D0} is the *zero-lift drag coefficient* and k is the *lift-induced drag coefficient factor*. While the zero drag coefficient contains the parasitic drag of the whole aircraft, the wing is mainly responsible for the lift-induced drag. Hence, we can intuitively consider the wing as a drag to lift converter.

Besides the choice of the airfoil, the aspect ratio of the wing plays an important role. It is also common to describe the lift-induced

coefficient k using the Oswald efficiency factor e ($e \leq 1$), which is a correction factor that reflects the deviation from an ideal elliptical lift distribution ($e = 1$). The relationship between k and e is:

$$k = \frac{1}{\pi A e} \quad (4)$$

where A is the aspect ratio of the wing. Data regarding aircraft geometry, including aspect ratio, is often published. For example, they are available in [Gunston \(2015\)](#). Parameter e is the Oswald factor that can be modeled theoretically as follows:

$$e = \frac{1}{Q + P\pi A} \quad (5)$$

where Q and P represents the inviscid and viscous part of the induced drag coefficient. There are many ways to approximate P and Q , which are summarized by [Niță and Scholz \(2012\)](#). In this paper, we have adopted the model proposed by [Kroo and Shevell \(2001\)](#) to calculate the Oswald efficiency factor (e), in which the Q parameter is approximated as:

$$Q = \frac{1}{0.99[1 - 2(d_f/b)^2]} \quad (6)$$

where d_f/b is the ratio of fuselage diameter to the wingspan. The P parameter is considered to be dependent on the zero-lift drag coefficient as:

$$P = 0.38C_{D0} \quad (7)$$

where the coefficient 0.38 was obtained empirically based on several existing aircraft types. Combining the previous equations, we can produce a closed-form model for the lift-induced drag coefficient:

$$k = \frac{1}{0.99[1 - 2(d_f/b)^2]\pi A} + 0.38C_{D0} \quad (8)$$

as well as the Oswald efficiency factor according to Eq. (4):

$$e = \left(\frac{1}{0.99[1 - 2(d_f/b)^2]} + 0.38C_{D0}\pi A \right)^{-1} \quad (9)$$

Now that the multi-level drag polar model is defined, the remaining challenge is to estimate the coefficients C_{D0} , e , and k . To do so, we will first estimate these coefficients under clean aerodynamic configuration (no flap deflections) and at low Mach number flight conditions. Since e and k are related to C_{D0} according to Eq. (8) and (9), we can only consider C_{D0} a independent variable in the estimation. However, C_{D0} is not the only unknown parameter for the entire estimation problem. For example, aircraft mass and thrust are other two unknowns, which are to be considered in the following section.

3. Estimation of the drag polar under clean configuration

In this section, we explore the principle of a novel hierarchical model that describes the total energy model in a stochastic fashion, where the model parameters are considered as random variables. Drag polar coefficients are then inferred based on ADS-B and Enhanced Mode S surveillance data. The clearest benefit of this stochastic total energy (STE) model is that the process can be applied to any aircraft, as long as accurate flight data is available, and the basic performance parameters of the aircraft, such as geometry and engines, are known. The following part of this section describes the estimation steps in detail.

3.1. The hierarchical stochastic model

In the total energy model, the change of energy is commonly described by multiplying each force with the speed in the corresponding direction. This results in the following equation:

$$(T_t - D_t)V_t = m_t a_t V_t + m_t g V S_t \quad (10)$$

where T and D are the thrust and drag of the aircraft, m is the aircraft mass. Parameters a , g , V , and VS are the acceleration, gravitational acceleration, airspeed, and vertical speed respectively. These are variables that can be derived from aircraft surveillance data. Subscript t indicates the data is a time series. In general, thrust can be modeled as a function of velocity and altitude. In this research, we use the thrust model proposed by [Bartel and Young \(2008\)](#). Let f_{thr} represent the function that gives the maximum thrust, the net thrust of the engines is expressed as:

$$T_t = \delta_T f_{thr}(V_t, h_t, VS_t) \quad (11)$$

where f_{thr} is the maximum thrust profile. δ_T represents the thrust setting. Combining the previous two equations, the drag coefficient is calculated as:

$$C_{D,t} = \frac{D_t}{q_t S} \quad (12)$$

$$= \frac{\delta_T f_{thr}(V_t, h_t, VS_t) - m_t a_t - m_t g VS_t / V_t}{qS} \quad (13)$$

It is also possible to derive the drag coefficient using the drag polar equation, according to Eq. (3). First, from the equilibrium of forces in the direction perpendicular to the airspeed, we find the relation between the lift coefficient and the mass:

$$C_{L,t} = \frac{L_t}{q_t S} = \frac{m_t g}{q_t S} \quad (14)$$

where the effects of flight path angle and bank angle are assumed to be neglectable. When it is combined with Eq. (8), the drag coefficient can also be expressed as:

$$\begin{aligned} C_{D,t}^* &= C_{D0} + k C_{L,t}^2 \\ &= C_{D0} + k \left(\frac{m_t g}{q_t S} \right)^2 \\ &= C_{D0} + \left(\frac{1}{0.99[1 - 2(d_F/b)^2]\pi A} + 0.38 C_{D0} \right) \left(\frac{m_t g}{q_t S} \right)^2 \end{aligned} \quad (15)$$

Assuming a perfect system and perfect observations, the two drag coefficients (C_D and C_D^*), should be the same at each time step, with the following relationship:

$$\Delta C_{D,t} = C_{D,t} - C_{D,t}^* = 0 \quad (16)$$

Although noise is inevitably present, Eq. (16) can be seen as the general goal of the estimator. In other words, when considering the estimation as a minimization problem, $C_{D,t} = C_{D,t}^*$ is the equality constraint required to produce the solution.

At this point, there are three sets of unknown parameters, which are C_{D0} , m_t , and $\delta_{T,t}$. In order to have an accurate estimation of C_{D0} , we need to know more about m_t and $\delta_{T,t}$. Unfortunately, this information is not available directly from the surveillance data. Even though we do not know the exact mass and thrust setting of each flight, some hypotheses can be assumed:

1. C_{D0} and k are constant and the same for all flights of the same aircraft model, under clean configuration, in low-speed incompressible airflow.
2. With basic aerodynamic knowledge, it is possible to identify the ranges of C_{D0} and k values.
3. The range of aircraft mass and thrust setting values can be found empirically.
4. Accurate surveillance data for a sufficient number of flights can be obtained, including trajectories, velocities, temperature, and wind conditions.

In the proposed STE model, we consider all parameters as random variables. The observable parameters are defined as follows:

$$\begin{aligned} V_t &\sim \mathcal{N}(\tilde{V}_t, \sigma_v^2) \\ a_t &\sim \mathcal{N}(\tilde{a}_t, \sigma_a^2) \\ VS_t &\sim \mathcal{N}(\tilde{V}S_t, \sigma_{vs}^2) \\ h_t &\sim \mathcal{N}(\tilde{h}_t, \sigma_h^2) \end{aligned} \quad (17)$$

Here, each parameter is assumed to be drawn from a normal distribution. \tilde{V}_t , \tilde{a}_t , $\tilde{V}S_t$, and \tilde{h}_t are the observed values at each time step respectively, and σ_v^2 , σ_a^2 , σ_{vs}^2 , and σ_h^2 are the variances for each variable. Models for the three sets of unknown system parameters can be constructed similarly:

$$\begin{aligned} \delta_{T,t} &\sim \mathcal{U}(\delta_{Tmin}, \delta_{Tmax}) \\ m_t &\sim \mathcal{U}(m_{min}, m_{max}) \\ C_{D0} &\sim \mathcal{U}(C_{D0min}, C_{D0max}) \end{aligned} \quad (18)$$

where $\delta_{T,t}$, m_t , and C_{D0} are defined with uniform probability density functions. Random variable $\delta_{T,t}$ and m_t are defined as thrust setting and mass at time t , where different random variables are used at different time-steps. Finally, ΔC_D from Eq. (16), can be expressed as:

$$\Delta C_D \sim \mathcal{N}(0, \sigma_\Delta^2) \quad (19)$$

With these variables defined, we have converted the deterministic total energy model to a hierarchical stochastic model. This STE model considers each parameter as a random variable and preserves the underlying structure among the observable parameters (a , V , VS , τ , h), forces (T and D), and system parameters (m , C_{D0} , and k), as defined in the total energy model. In Fig. 1, the dependencies among all these parameters are visualized. In total, this hierarchical model includes ten random variables, which are indicated in gray.

Parameter values of the prior distributions defined in Eq. (17) and (18) (also in Fig. 1) are listed in Table 1. Variances for speed, vertical rate, and altitude are selected based on uncertainties defined by the ADS-B navigation accuracy category (RTCA, 2011). Mass is chosen to be uniformly distributed between the minimum operational weight and maximum takeoff weight. Other prior parameters are chosen empirically.

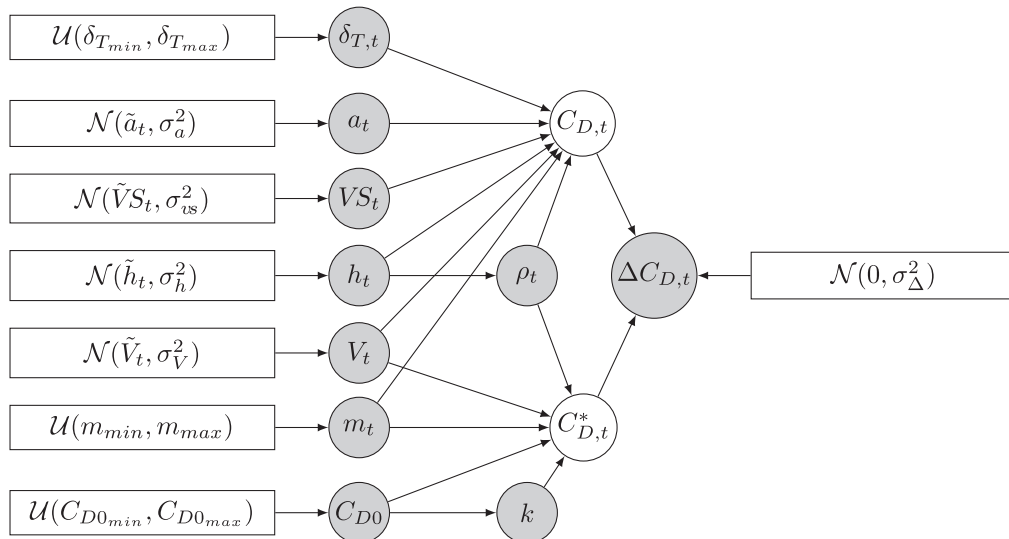


Fig. 1. Hierarchical relationships of model parameters.

Table 1
STE model hierarchical parameters.

Parameter	σ_v	σ_a	σ_{vs}	σ_h	δ_{Tmin}	δ_{Tmax}	m_{min}	m_{max}	C_{D0min}	C_{D0max}
Value	5	0.2	7.62	22.5	0.85	0.15	m_{OEW}	m_{MTOW}	0	0.05
Unit	m/s	m/s ²	m/s	m	–	–	kg	kg	–	–

3.2. Bayesian computing - Markov Chain Monte Carlo

With this hierarchical system where states are considered as random variables, we have converted the original estimation to a Bayesian minimization problem. Based on the prior probability of all model parameters, this approach allows us to compute the posterior probabilities based on the constraints in Eq. (16). To simplify the expression, let us define θ and \mathbf{y} as follows:

$$\begin{aligned}\theta &= \{C_{D0}, k, [\delta_{T,t}], [m_t], [V_t], [a_t], [VS_t], [h_t]\} \\ \mathbf{y} &= \{[\Delta C_{D,t}]\}\end{aligned}\quad (20)$$

where parameters in brackets have multiple dimensions. The goal of the estimation is to compute the joint posterior probability $p(\theta|\mathbf{y})$, which is difficult (and impractical) to obtain analytically due to the number of state variables. Instead, we use a Markov Chain Monte Carlo (MCMC) simulation to approach this numerically.

The MCMC method uses sequential sampling, drawing a large number of values of θ from approximate distributions and then correcting these draws based on the distribution constructed from previous values drawn. The final estimates can be obtained once the Markov Chain converges to a unique stationary distribution.

The simplest form of the MCMC sampling method is the Metropolis algorithm (Metropolis et al., 1953), which can be applied to almost any Bayesian computation problem. The algorithm can be explained in simple steps, which also demonstrate the principles of MCMC sampling. These steps are as follows:

1. Choose an initial set of θ as θ^0 .
2. For iteration $i = 1, 2, \dots, N$:
 - (a) Sample a proposal θ^* from a *jumping distribution* $J(\theta^*|\theta^{i-1})$, which is a conditional probability dependent on the current set of values. The jumping distribution is usually chosen as a normal distribution with θ^{i-1} as the mean.
 - (b) Calculate the ratio using the Bayes' rule:

$$r = \frac{P(\theta^*|\mathbf{y})}{P(\theta^{i-1}|\mathbf{y})} = \frac{P(\theta^*)P(\mathbf{y}|\theta^*)}{P(\theta^{i-1})P(\mathbf{y}|\theta^{i-1})}\quad (21)$$

where $P(\theta^*)$ is defined by the prior distributions, and the likelihood $P(\theta^{i-1}|\mathbf{y})$ is computed based on the hierarchical model.

- (c) set θ^i as θ^* with probability of $\min(r, 1)$, otherwise keep as θ^{i-1} .

When the MCMC chain reaches the desired number of iterations, the sampling process can be stopped. The values from each iteration stored in the Markov Chain are used to construct the posterior distributions of the model parameters.

The Metropolis sampler is simple to implement and can be applied to both continuous and discrete probability distributions. A drawback is that it can lead to a very long convergence run-time, due to the random-walk behavior. More efficient ways of sampling have been built upon the Metropolis sampling (Gelman et al., 1996; Neal, 1994). However, the fundamental concept is similar among different types of samplers. Essentially, with iterations, the MCMC sampler must choose the next set of parameters based on how likely all parameters satisfy the observations.

In the experiments of this paper, a new sampler called No-U-Turn Sampler (NUTS) is used (Hoffman and Gelman, 2014). The NUTS sampler is an improved Hamiltonian Monte Carlo which avoids the random walk behavior. It also implements a set of procedures allowing sampler hyper-parameters to be determined automatically and, thus, allows the Markov Chains to converge quickly with fewer sampling iterations.

3.3. Obtaining the posterior estimates

Using the NUTS sampler, the convergence of the Markov Chains can usually be achieved within 1,000 iterations. In our experiments, we have increased the number of iterations to 3,000 to have a larger number of stable samples. Once a sufficient number of sampling iterations has been reached, it is possible to compute the posterior probability density function using the numerical approximation based on these samples. An example can be seen in Fig. 6 in the experiment section later in this paper.

The mean of the samples representing C_{D0} and k are considered as the final estimates for the drag polar parameters. The standard deviation for samples representing C_{D0} is also calculated.

In some cases, errors occur in decoded surveillance data, which may lead to solutions converged at boundary conditions. Based on the mean and standard deviation of the posterior distribution of C_{D0} , we construct the following relationship to determine the validity of a solution:

$$\hat{C}_{D0} - 2\hat{\sigma}_{C_{D0}} > C_{D0min} \quad (22)$$

$$\hat{C}_{D0} + 2\hat{\sigma}_{C_{D0}} < C_{D0max} \quad (23)$$

where \hat{C}_{D0} and $\hat{\sigma}_{C_{D0}}$ are mean and standard deviation from the posterior distribution.

4. Effects of different aerodynamic configurations and high Mach numbers

As discussed earlier, the estimated drag polar is valid only for clean aircraft configuration and incompressible airflow. A change in the shape of an aircraft can alter the drag polar. The most notable changes in aircraft configuration involve flaps (and slats), speed brakes (or lift dumpers), and landing gear. Each structural setting, here, has its own corresponding drag polar model. In this paper, we focus on the additional drag caused by flaps and landing gear. When aircraft flies at higher Mach numbers, the compressibility effect also alters the drag polar. Thus, the wave drag is also modeled in this section.

4.1. Flaps

Flaps are deployed to provide an increase in the maximum lift coefficient. They are often deployed to allow aircraft to fly at lower speeds with a higher lift, typically at low altitudes (for example during takeoff, initial climb, and approach). Different aircraft types have different configurations of flaps and flap settings. In general, an increase in flap angle leads to an increase in the lift coefficient under the same angle of attack, at the expense of higher drag. Slats are similar to flaps but located on the leading edge of the wing. They increase the maximum lift coefficient by increasing the stall angle of attack. Slats are automatically extended when selecting a flap setting and are considered as part of this configuration. Different flap designs have been adopted by aircraft manufacturers. In Table 2, a list of common flap options on airfoils and their approximated maximum lift coefficients are listed. These values are produced by Loftin (1985). It is worth noting that the $C_{L,max}$ values of an airfoil are larger than the values of the aircraft with the same shaped wing, especially for swept wings (Anderson, 1999, p.263).

The increase in lift coefficient due to flap deflection can be calculated empirically, based on data from the literature (Torenbeek, 1976, p.253). This accounts for the effect of the change in the wing area, as well as the changes in shape and camber. The deflection angle of flaps (δ) and increased maximum lift coefficient $C_{L,max}$ are shown in Table 3, where IC and FA represent the initial climb and final approach configuration respectively.

With flaps deflected, the drag of the wing also increases. Using an empirical model (McCormick, 1995, p.109), this increase in drag coefficient due to flaps deflection can be computed as:

$$\Delta C_{D,f} = \lambda_f \left(\frac{c_f}{c} \right)^{1.38} \left(\frac{S_f}{S} \right) \sin^2 \delta_f \quad (24)$$

where c_f/c and S_f/S are flap to wing chord ratio and flap to wing surface ratio respectively. δ_f is the flap deflection angle. When exact c_f/c and S_f/S are not available, they are both assumed to be 0.15, which is a simplified empirical approximation. λ_f is dependent on the type of flaps. According to McCormick (1995), λ_f is set to be 1.7 for plain and split flaps, and 0.9 for slotted flaps.

The deflection of flaps also affects the Oswald efficiency factor (e). Based on data from several existing aircraft, a linear relationship is found by Obert (2009). The model to calculate such increase in e is:

Table 2
Example flap settings in airfoils (Loftin, 1985, p.107).









Flap types	$C_{L,max}$	Illustration
airfoil only	1.4	
leading-edge slat	2.4	
plain flap	2.5	
split flap	2.6	
Fowler single-slotted flap	2.9	
Fowler multi-slotted flap	3.0	
with leading-edge slat	3.3	
with boundary layer suction	3.9	

Table 3
Increase of lift coefficient with flaps with typically flap deflection angles.

Trailing	Leading	δ_{IC}	δ_{FA}	$C_{L,max,IC}$	$C_{L,max,FA}$
plain flap		20°	60°	1.60	2.00
split flap		20°	40°	1.70	2.20
single-slotted flap		15°	40°	2.20	2.90
double-slotted flap		20°	50°	1.95	2.70
double-slotted flap	w/ slat	20°	50°	2.60	3.20
triple-slotted flap	w/ slat	20°	40°	2.70	3.50

$$\Delta e_f = 0.0046\delta_f \quad (\text{for rear-mounted engines})$$

$$\Delta e_f = 0.0026\delta_f \quad (\text{for wing-mounted engines}) \quad (25)$$

4.2. Landing gears

When extended, the landing gear adds a significant amount of drag to the aircraft. Hence, the landing gear is retracted as soon as the aircraft becomes airborne and only extended shortly before landing. There are limited studies that quantify the drag coefficient of aircraft landing gears. In this paper, we adopt the model proposed by Mair (1996) to calculate the increased drag coefficient caused by landing gears:

$$\Delta C_{D,g} = \frac{W}{S} K_{uc} m_{\max}^{-0.215} \quad (26)$$

Here, W/S is the wing loading, m_{\max} refers to the maximum mass of an airplane, and K_{uc} is a factor that relates to the flap deflection angle. In principle, the value of K_{uc} is lower when more flap deflection is applied. This is because the flow velocity along the bottom of the wing decreases when flaps are deployed, which leads to a lower drag on the landing gear. For simplification, it is taken as 3.16×10^{-5} in this paper, based on values given by Mair (1996).

4.3. Wave drag at high Mach numbers

When aircraft fly at a high Mach number, the compressibility of the airflow also needs to be considered. Under such conditions, the drag can increase drastically due to local supersonic flows and corresponding shock waves. Modern airliners often cruise at transonic speeds, where the additional wave drag should not be ignored when calculating the total drag.

To model this wave drag, we first need to estimate the critical Mach number (M_{crit}), which is defined as the lowest Mach number at which the airflow over any part of the aircraft reaches the speed of sound. The critical Mach number can often be related to the drag divergence Mach number, which is the Mach number where the drag starts to increase rapidly with increasing aircraft speed.

According to Mason (1990), the drag divergence Mach number can be approximated as:

$$M_{dd} = \frac{\kappa_A}{\cos \Lambda} - \frac{t/c}{\cos^2 \Lambda} - \frac{C_L}{10 \cos^3 \Lambda} \quad (27)$$

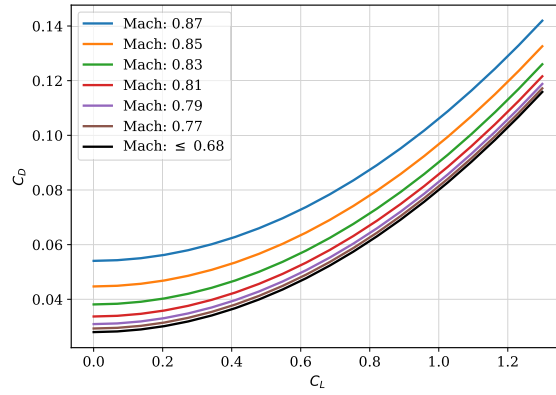


Fig. 2. Changes of drag polar due to compressibility.

where Λ is the mid-chord sweep angle. t/c is the thickness ratio. κ_A is the Korn factor, which is set to be 0.95 for supercritical wing profiles and 0.87 for conventional wing profiles. C_L is the maximum lift coefficient available, which is empirically considered to be around 1.3 in this paper. When a value for t/c is not available for an aircraft type, a default common value of 0.11 is used, based on empirical data from Obert (2009).

Knowing the drag divergence Mach number, the critical Mach number can be calculated as follows, according to (Gur et al., 2010):

$$M_{\text{crit}} = M_{\text{dd}} - \sqrt[3]{\frac{0.1}{80}} \quad (28)$$

When combining Eq. (28) and Eq. (27), the final closed-form critical Mach number model can be found:

$$M_{\text{crit}} = \frac{\kappa_A}{\cos \Lambda} - \frac{t/c}{\cos^2 \Lambda} - \frac{C_L}{10 \cos^3 \Lambda} - \sqrt[3]{\frac{0.1}{80}} \quad (29)$$

Finally, according to Inger (1993) and Gur et al. (2010), the rise of the drag coefficient due to the wave drag is modeled as:

$$\Delta C_{D,w} = \begin{cases} 0 & M \leq M_{\text{crit}} \\ 20(M - M_{\text{crit}})^4 & M > M_{\text{crit}} \end{cases} \quad (30)$$

As an example, in Fig. 2, the drag polars of the Boeing 747-400 aircraft under different Mach numbers are illustrated.

4.4. The combined drag polar model

Considering different structural variations such as flap deflection and deployment of the landing gear, as well as the effect of the wave drag beyond the critical Mach number, the dynamic zero-lift drag coefficient C_{D0}^* is modeled as:

$$C_{D0,\text{total}} = C_{D0} + \Delta C_{D,f} + \Delta C_{D,g} + \Delta C_{D,w} \quad (31)$$

Similarly, considering the flap deflections, the dynamic Oswald factor is modeled as:

$$e_{\text{total}} = e + \Delta e_f \quad (32)$$

while the lift-induced drag coefficient becomes:

$$k_{\text{total}} = \frac{1}{1/k + \pi A \Delta e_f} \quad (33)$$

We can see that $\Delta C_{D,f}$, $\Delta C_{D,g}$, $\Delta C_{D,w}$, and Δe_f can all be attributed to the aircraft design, which is mostly related to the parameters of wings.

5. Experiments

The experiment consists of several parts. We start with an example of drag polar estimation based on a single trajectory. Then, the results from multiple trajectories and aircraft types are summarized. Later on, we also include a comparative analysis between the estimation results and drag polar obtained from CFD simulations.

A dataset of around 100 climbing flights per aircraft type is collected using a Mode S receiver set up at the Delft University of Technology. The observed flights were taking off from Amsterdam Schiphol airport during March 2018. Fig. 3 shows the ground tracks and vertical profiles of a selected subset of these flights.

Besides the ground speed obtained from ADS-B, real-time wind data are computed using the Meteo-Particle model proposed by Sun et al. (2018b). Combining ground speed and accurate wind information, the airspeed of the aircraft is computed. The use of true

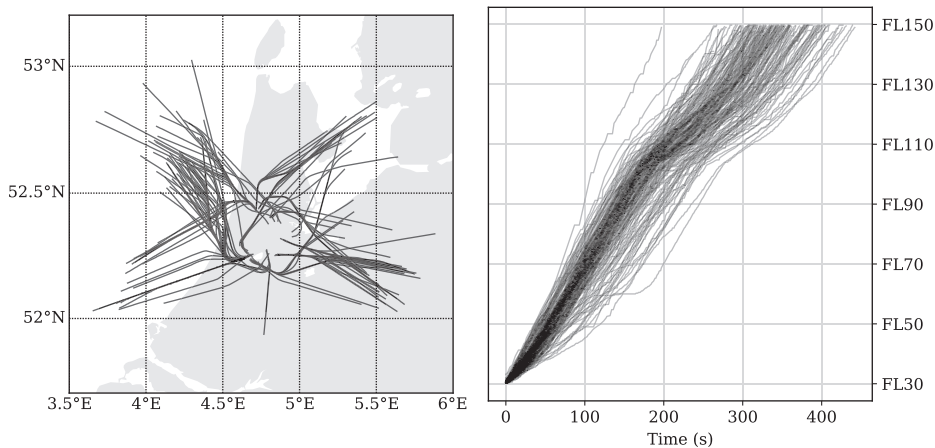


Fig. 3. The trajectories of the Boeing 747-400 flights (during March 2018, departing from Schiphol airport).

airspeed instead of ground speed allows us to describe the performance more accurately.¹

For each flight, we apply MCMC sampling with the STE model to obtain the posterior probability distribution of the parameters C_{D0} and k . Using the NUTS MCMC implementation by the PyMC3 library (Salvatier et al., 2016), we can conveniently perform the sampling of our model with predefined prior distributions. To ensure consistent convergence, we utilize four independent chains, which are sampled in parallel.

5.1. Estimation of the drag polar using the STE model and MCMC sampling

First, a random example flight from the dataset is selected to illustrate the estimation process based on one flight. In Fig. 4, the altitude and speed profiles of this flight are shown.

In Fig. 5, the traces of four chains (on the right-hand side) and the estimated posterior density (on the left-hand side) are shown. Each chain is marked with a different color. As shown on the left-hand side of Fig. 5, in all four independent chains, similar posterior densities are produced for C_{D0} and k respectively.

The similar posterior densities from different Markov Chains indicate the stable convergences of the sampling process. Combining all chains, we can obtain the mean value C_{D0} and k from the posterior distribution, which is shown in Fig. 6.

5.2. Multiple aircraft types

Next, we extend the experiment to all flights gathered in the previously-mentioned dataset, which contains flights of 20 common aircraft types. Based on these flights, we can obtain C_{D0} and k for each aircraft type by combining the results of all flights. In Fig. 7, the distributions of C_{D0} and k are shown.

Most of the C_{D0} values are between 0.02 and 0.04, while the values for k are mostly between 0.035 and 0.055. In Table 4, all these values are listed in detail together with other related aerodynamic parameters.

5.3. Comparison with CFD simulation results

Due to the lack of validation data from the aircraft manufacturers, one way to verify the results of the proposed MCMC method is to conduct simple CFD simulations based on available open 3D models of the aircraft. In this section, a series of CFD simulations for a Boeing 747-400 aircraft² are conducted using OpenFOAM (Jasak et al., 2007).

Two different configuration scenarios are simulated, where one scenario does not include any engines, while the other includes all engines. In Fig. 8, these different configurations are shown.

In the first scenario, due to the removal of the engines, the drag is reduced when compared to normal operational conditions. In the second scenario, the engines are considered as enclosed objects, where no airflow passes the engine. As such, higher drag in the CFD simulation is expected to be produced. The hypothesis is that the actual drag should be between these two results.

With these two different scenarios, CFD calculations are run under different angles of attack, ranging from -5 degrees to 30 degrees. All CFD simulations are conducted with a free stream speed of approximately 0.3 Mach. For each case, drag and lift coefficients (C_D and C_L) are computed. In Fig. 9, results from all rounds of the simulations are shown.

¹ Though true airspeed information also exists in Mode S Enhanced Surveillance communication, its update rate is much less than the ground speed from ADS-B. Hence, we use of derived airspeed data based on ADS-B ground speed and wind field information.

² This open 3D model is retrieved from: <http://hangar.openvsp.org/vspfiles/184>, on October, 2018.

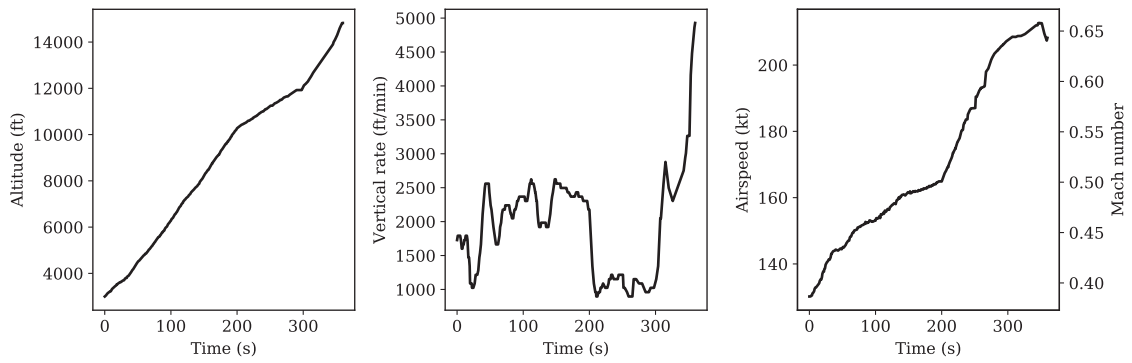


Fig. 4. Altitude and speed profiles of the Example 747-400 flight.

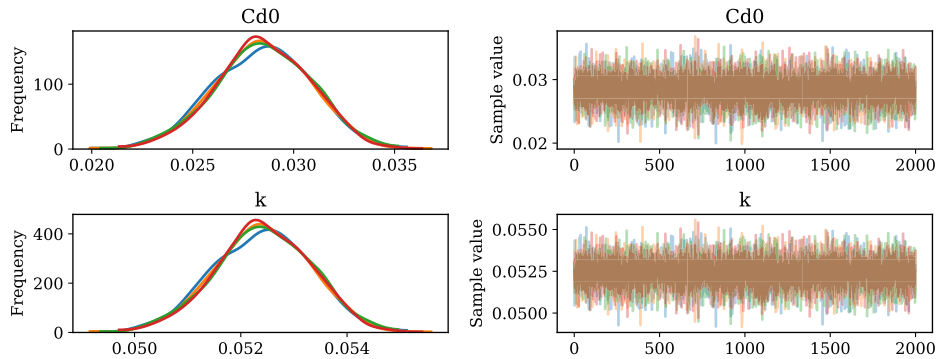


Fig. 5. MCMC sampling of a Boeing 747-400 flight.

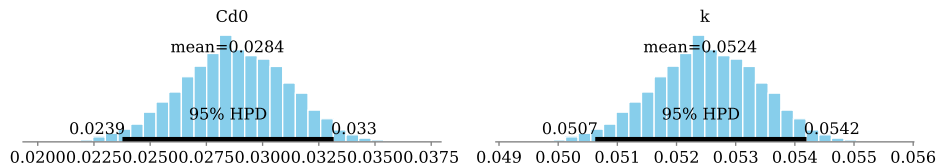


Fig. 6. Posterior distribution of C_{D0} and k from MCMC sampling.

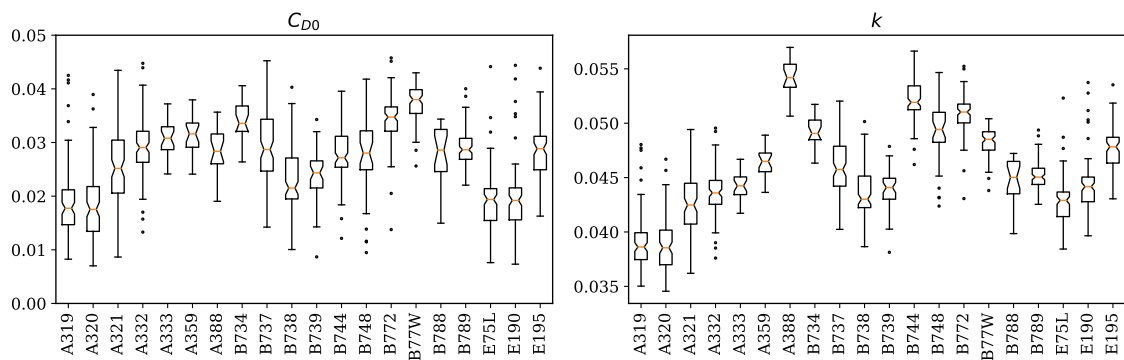


Fig. 7. Drag polar of common aircraft models based on multiple flights.

We can plot the relationship between the drag and lift coefficient by removing the variable of the angle of attack. The result is shown in Fig. 10. In this figure, quadratic drag polars are fitted to these data points with angles less or equal than 15 degrees. The drag polar obtained from the previous STE-MCMC approach is also shown in solid black lines. We can see that the actual drag polar computed based on flight data lies between the results from the two CFD scenarios. This is a positive verification for the drag polar obtained based on the STE model.

Table 4
Drag polar and related coefficients.

Aircraft	Aircraft type	C_{D0}	k	e	M_{crit}	λ_f	c_f/c	S_f/S	$\Delta C_{D,g}$
A319	Airbus A319	0.019	0.039	0.793	0.63	0.90	0.18	0.17	0.017
A320	Airbus A320	0.018	0.039	0.798	0.63	0.90	0.18	0.17	0.017
A321	Airbus A321	0.026	0.043	0.746	0.63	0.90	0.18	0.16	0.019
A332	Airbus A330-200	0.029	0.044	0.728	0.64	0.90	0.15	0.15	0.014
A333	Airbus A330-300	0.030	0.044	0.719	0.64	0.90	0.15	0.15	0.014
A359	Airbus A350-900	0.031	0.046	0.725	0.65	0.90	0.15	0.15	0.013
A388	Airbus A380-800	0.028	0.054	0.781	0.69	0.90	0.15	0.15	0.012
B734	Boeing 737-400	0.034	0.049	0.705	0.61	0.90	0.15	0.15	0.021
B737	Boeing 737-700	0.029	0.046	0.736	0.63	0.90	0.15	0.15	0.016
B738	Boeing 737-800	0.023	0.044	0.775	0.63	0.90	0.15	0.15	0.017
B739	Boeing 737-900	0.024	0.044	0.769	0.63	0.90	0.15	0.15	0.018
B744	Boeing 747-400	0.028	0.052	0.774	0.68	0.90	0.20	0.15	0.015
B748	Boeing 747-8	0.027	0.049	0.771	0.68	0.90	0.19	0.14	0.015
B772	Boeing 777-200	0.034	0.051	0.723	0.65	0.90	0.17	0.16	0.014
B77W	Boeing 777-300ER	0.037	0.048	0.687	0.65	0.90	0.16	0.15	0.016
B788	Boeing 787-8	0.027	0.045	0.748	0.67	0.90	0.15	0.15	0.013
B789	Boeing 787-9	0.029	0.045	0.737	0.67	0.90	0.15	0.15	0.014
E75L	Embraer E175 (LR)	0.019	0.043	0.803	0.63	0.90	0.15	0.15	0.017
E190	Embraer E190 (LR)	0.019	0.044	0.813	0.63	0.90	0.15	0.15	0.016
E195	Embraer E195 (LR)	0.028	0.048	0.752	0.63	0.90	0.15	0.15	0.017

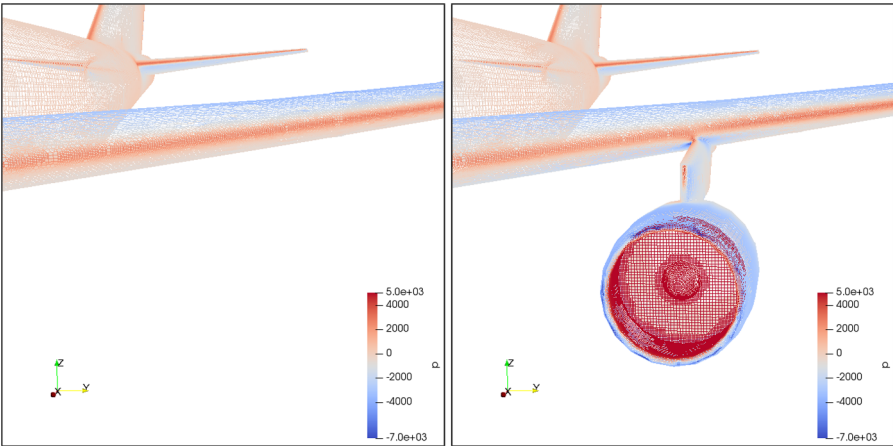


Fig. 8. Two CFD scenarios. Colors indicate different levels of calculated air pressure distributed around the body.

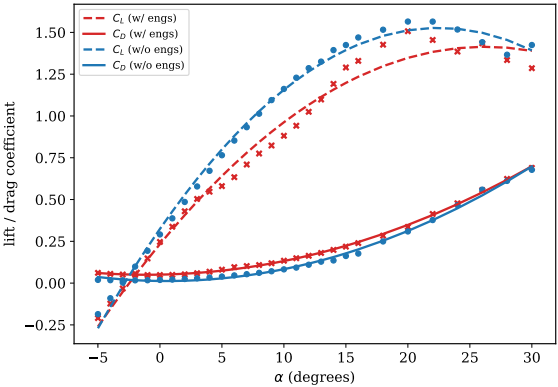


Fig. 9. Lift and drag coefficients as functions of angle of attack based on CFD simulations.

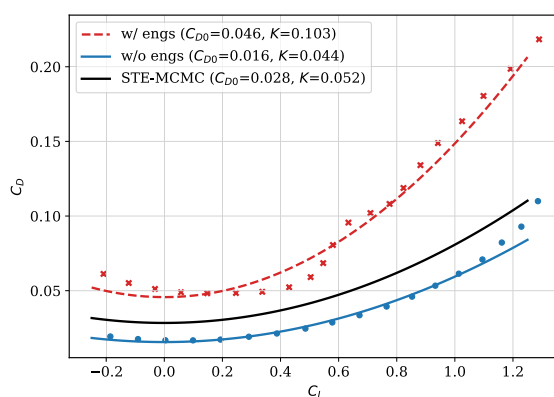


Fig. 10. Relationships of lift and drag coefficients.

6. Summary and discussion

6.1. Drag polar for different aircraft types

In Table 4, the drag polars of the 20 common aircraft types are listed. This table shows the zero-lift drag coefficient (C_{D0}), lift-induced drag coefficient factor (k), and Oswald efficiency factor (e), which are all estimated using the MCMC and STE model. For non-clean configuration situations, we can use the previously introduced empirical models to incorporate changes of drag polar coefficients due to flap or landing gear deployment. Combining the coefficients from Table 4 and Eq. (24), the increased drag coefficient at different flap deflection angles can be calculated. Similarly, the change in the Oswald factor can be calculated according to Eq. (25). The increased values of the drag coefficient due to landing gear deployment are also listed in this table. In addition, the approximated critical Mach number is given in Table 4 as well.

To facilitate future studies that rely on drag polar models, a pre-computed table with a set of drag polars under non-clean configuration with fixed flap deflection angles at the initial climb and landing phases are computed and listed in Table 5.

6.2. Comparison with BADA models

Due to the restriction of the BADA license, exposure of specific BADA coefficients is not permitted. Instead of showing the exact difference between BADA and our model for each aircraft type, the overall statistics for all available aircraft are shown in Fig. 11.

The mean absolute difference for C_{D0} and k are found to be around 0.007. This gives a good indication of what the level of difference in the outcome of this study is, compared to well-established performance models. However, we should be cautious when interpreting the difference. The difference between the two models does not directly represent the accuracy of the proposed drag polars in this paper, but it indicates the degree of variations with existing model.

Table 5

Drag polar coefficients in non-clean configurations with default flaps deflection angles.

Aircraft	$\delta_{f,IC}$	$C_{D0,IC}$	k_{IC}	e_{IC}	$\delta_{f,FA}$	$C_{D0,FA}$	k_{FA}	e_{FA}
A319	20°	0.021	0.037	0.845	40°	0.025	0.035	0.897
A320	20°	0.020	0.036	0.850	40°	0.024	0.034	0.902
A321	20°	0.028	0.040	0.798	50°	0.034	0.036	0.876
A332	20°	0.030	0.041	0.780	50°	0.035	0.037	0.858
A333	20°	0.032	0.041	0.771	50°	0.036	0.037	0.849
A359	20°	0.032	0.043	0.777	50°	0.037	0.039	0.855
A388	20°	0.030	0.051	0.833	40°	0.033	0.048	0.885
B734	20°	0.036	0.046	0.757	40°	0.038	0.043	0.809
B737	20°	0.030	0.043	0.788	50°	0.035	0.039	0.866
B738	20°	0.024	0.041	0.827	50°	0.029	0.037	0.905
B739	20°	0.025	0.041	0.821	50°	0.030	0.038	0.899
B744	20°	0.030	0.049	0.826	40°	0.034	0.046	0.878
B748	20°	0.029	0.046	0.823	40°	0.032	0.043	0.875
B772	20°	0.036	0.047	0.775	50°	0.041	0.043	0.853
B77W	20°	0.039	0.045	0.739	50°	0.044	0.041	0.817
B788	20°	0.029	0.042	0.800	40°	0.031	0.039	0.852
B789	20°	0.030	0.042	0.789	40°	0.033	0.040	0.841
E75L	20°	0.020	0.040	0.855	50°	0.025	0.037	0.933
E190	20°	0.020	0.041	0.865	50°	0.025	0.038	0.943
E195	20°	0.029	0.045	0.804	50°	0.034	0.041	0.882

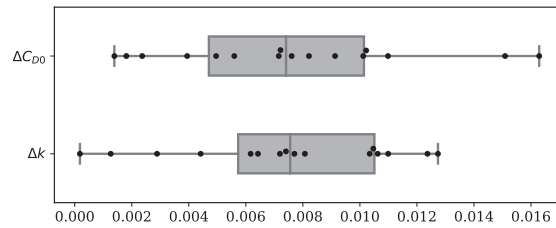


Fig. 11. Absolute difference of drag polar between BADA (version 3.12) and the model derived in this paper under clean configuration.

6.3. Uncertainties

It should be noted that, in the proposed hierarchical model, all parameters are considered as random variables (described by probability density functions) instead of scalar values. Most parameters (except C_{D0} and k) are also expressed as time-varying random variables. The time-series variables are constructed as multi-dimensional probability density functions. The solution of this hierarchical stochastic model is possible thanks to numerical approximation using the Markov Chain Monte Carlo (MCMC) techniques.

In the proposed STE aircraft performance model, two major sources of uncertainty exist, which are the aircraft mass and the thrust. We consider the mass as a uniformly distributed random variable at each time step. Unlike the informed mass assumption addressed in Sun et al. (2018a), the uniformed distribution considers all masses as equally possible. It is sampled together with all other parameters. When evaluating the sampling results, we can illustrate the posterior distribution of mass at different time steps, as shown in Fig. 12. In this paper, the goal is to estimate the drag polar coefficients C_{D0} and k , while considering the uncertainties of aircraft mass. The posterior distributions can be thought of as the results that optimize all different parameters at all time steps.

The aircraft thrust model is the factor that influences the results the most while using the STE model, as the thrust is strongly correlated to the drag of the aircraft. The uncertainty in thrust can be categorized in two ways. First, aircraft may be equipped with different engine options within the same aircraft type family. This paper uses a default engine per aircraft type (shown in Table 6), which can cause a small level of uncertainty. The second cause of uncertainty is related to the thrust model used in this paper. We implement the thrust model based on two-shaft turbofan engines (Bartel and Young, 2008), according to which, the model has an

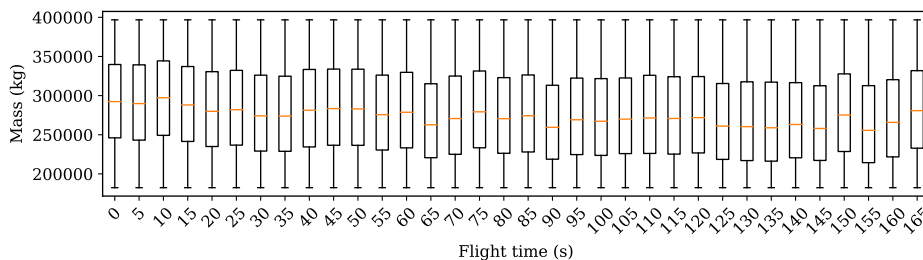


Fig. 12. The distributions of mass at different flight time steps.

Table 6
Default engine and maximum thrust for each aircraft type.

Aircraft	Default engine	Maximum thrust
A319	V2522-A5	102 kN
A320	CFM56-5A3	117 kN
A321	CFM56-5B1	133 kN
A332	Trent 772	320 kN
A333	Trent 772	320 kN
A359	Trent XWB-84	379 kN
A388	Trent 970-84	338 kN
B734	CFM56-3B-2	98 kN
B737	CFM56-7B26	116 kN
B738	CFM56-7B26	116 kN
B739	CFM56-7B26	116 kN
B744	RB211-524G	253 kN
B748	GE90-115B	299 kN
B772	Trent 895	413 kN
B77w	GE90-115B	513 kN
B788	Trent 1000-C2	334 kN
B789	Trent 1000-K2	350 kN
E751	CF34-8E6	59 kN
E190	CF34-10E5	77 kN
E195	CF34-10E5	77 kN

uncertainty of 4.5% of the maximum thrust when compared to engine performance data. The uncertainty in the thrust model undoubtedly will affect the final uncertainty of the drag polar estimates. Since it is hard to accurately describe this uncertainty in thrust, a uniform probability density function with large bounds is considered for the thrust setting (δ_T). In this way, the possible variations in thrust setting due to different procedures can be considered by this parameter.

7. Conclusion

In this paper, we proposed a method to derive the aircraft drag polar based on a point-mass performance model. A novel stochastic total energy model was developed to estimate drag polar coefficients using publicly available ADS-B and Enhanced Mode S surveillance data. Based on this information, the drag polar for aircraft could be estimated under the clean aerodynamic configuration. By considering the states in the total energy model as random variables, we transformed the estimation to a problem that could be solved with the Bayesian method, where the solution of such a minimization problem was derived using the Markov Chain Monte Carlo method. Compared to deterministic minimization methods, our approach not only yielded estimations but also provided the posterior probability densities for the states to be estimated.

Based on studies from literature, we also included the models that can be used to compute additional drag caused by flaps, landing gear, and wave drags. Combining all this knowledge, the drag polar model proposed in this paper can describe different aerodynamic configurations at different flight phases, including takeoff, climb, descent, approach, and landing.

One of the major challenges in this study was to find proper alternative data sources that could be used to validate and improve the obtained drag polars. Due to the limited amount of public information related to aerodynamic properties of modern commercial aircraft, there are still uncertainties in the results that could be explored in follow-on studies. One possible consideration for future research is to use accurate flight management system data to improve the estimation results.

A list of drag polars for the 20 most common aircraft types was produced in this paper. To the best of our knowledge, this is the first time such a wide range of modern aircraft drag polar models have been derived and shared publicly. The resulting drag polars proposed in this paper have been implemented in the Open Aircraft Performance Model (OpenAP),³ which was also used to support the open-source air traffic simulator BlueSky⁴ (Hoekstra and Ellerbroek, 2016). With the open-source license, we believe the drag polar coefficients produced with the method presented in this paper can contribute to improved transparency, accessibility, and repeatability among future air transportation studies.

Appendix A. Supplementary material

Supplementary data associated with this article can be found, in the online version, at <https://doi.org/10.1016/j.trc.2020.01.026>.

References

- Anderson, J.D., 1999. Aircraft Performance and Design. McGraw-Hill Science/Engineering/Math.
- Bartel, M., Young, T.M., 2008. Simplified thrust and fuel consumption models for modern two-shaft turbofan engines. *J. Aircraft* 45 (4), 1450–1456.
- Gelman, A., Roberts, G.O., Gilks, W.R., et al., 1996. Efficient metropolis jumping rules. *Bayesian Stat.* 5, 599–608.
- Gunston, B., 2015. Jane's all the World's Aircraft: Development and Production: 2015–16. IHS Global.
- Gur, O., Mason, W.H., Schetz, J.A., 2010. Full-configuration drag estimation. *J. Aircraft* 47 (4), 1356–1367.
- Hoekstra, J.M., Ellerbroek, J., 2016. BlueSky ATC simulator project: an open data and open source approach. In: 7th International Conference on Research in Air Transportation, pp. 1–8.
- Hoerner, S.F., 1951. Aerodynamic Drag: Practical Data on Aerodynamic Drag Evaluated and Presented. Otterbein Press.
- Hoerner, S.F., 1958. Fluid-dynamic Drag: practical information on aerodynamic drag and hydrodynamic resistance. Hoerner Fluid Dyn.
- Hoffman, M.D., Gelman, A., 2014. The no-u-turn sampler: adaptively setting path lengths in hamiltonian monte carlo. *J. Mach. Learn. Res.* 15 (1), 1593–1623.
- Inger, G., 1993. Application of oswatitsch's theorem to supercritical airfoil drag calculation. *J. Aircraft* 30 (3), 415–416.
- Jasak, H., Jemcov, A., Tukovic, Z., et al., 2007. Openfoam: A C++ library for complex physics simulations. In: International Workshop on Coupled Methods in Numerical Dynamics, vol. 1000. IUC Dubrovnik Croatia, pp. 1–20.
- Kroo, I., Shevell, R., 2001. Aircraft Design: Synthesis and Analysis. Desktop Aeronautics Inc., Textbook Version 0.99.
- Loftin, L.K., 1985. Quest for Performance: The Evolution of Modern Aircraft. Scientific and Technical Information Branch. National Aeronautics and Space Administration.
- Mair, W., 1996. Aircraft performance, vol. 5 Cambridge University Press.
- Mason, W., 1990. Analytic models for technology integration in aircraft design. In: Aircraft Design, Systems and Operations Conference. p. 3262.
- McCormick, B.W., 1995. Aerodynamics, Aeronautics, and Flight Mechanics, vol. 2 Wiley, New York.
- Metropolis, N., Rosenbluth, A.W., Rosenbluth, M.N., Teller, A.H., Teller, E., 1953. Equation of state calculations by fast computing machines. *J. Chem. Phys.* 21 (6), 1087–1092.
- Nagel, J.B., Sudret, B., 2015. Bayesian multilevel model calibration for inverse problems under uncertainty with perfect data. *J. Aerospace Inform. Syst.* 12 (1), 97–113.
- Neal, R.M., 1994. An improved acceptance procedure for the hybrid monte carlo algorithm. *J. Comput. Phys.* 111 (1), 194–203.
- Niță, M., Scholz, D., 2012. Estimating the Oswald Factor from Basic Aircraft Geometrical Parameters. Deutsche Gesellschaft für Luft-und Raumfahrt-Lilienthal-Oberth eV.
- Obert, E., 2009. Aerodynamic Design of Transport Aircraft. IOS Press.
- RTCA, 2011. Minimum operational performance standards for 1090mhz extended squitter automatic dependent surveillance-broadcast (ads-b) and traffic information services-broadcast (tis-b)[j]. RTCA DO-260B with Corrigendum 1 (1), 1365–1372.
- Ruigrok, G., 2009. Elements of Airplane Performance, vol. 2 Delft Academic Press.
- Salvatier, J., Wiecki, T.V., Fonnesbeck, C., 2016. Probabilistic programming in python using pymc3. *PeerJ Comput. Sci.* 2, e55.
- Sun, J., Ellerbroek, J., Hoekstra, J., 2018a. Aircraft initial mass estimation using Bayesian inference method. *Transp. Res. Part C: Emerg. Technol.* 90, 59–73.
- Sun, J., Vũ, H., Ellerbroek, J., Hoekstra, J.M., 2018b. Weather field reconstruction using aircraft surveillance data and a novel meteo-particle model. *PLOS ONE* 13 (10), 1–33.
- Torenbeek, E., 1976. Synthesis of Subsonic Airplane Design. Delft University Press.
- van Es, G.W.H., 2002. Rapid estimation of the zero-lift drag coefficient of transport aircraft. *J. Aircraft* 39 (4), 597–599.

³ OpenAP includes all drag polar data, available at: <https://github.com/junzis/openap>.

⁴ BlueSky can be downloaded at: <https://github.com/tudelft-cns-atm/bluesky>.